Materials Advances

ROYAL SOCIETY OF CHEMISTRY

PAPER

View Article Online
View Journal | View Issue

Cite this: *Mater. Adv.*, 2023, 4, 6655

Approaching the minimum lattice thermal conductivity in TiCoSb half-Heusler alloys by intensified point-defect phonon scattering†

Ajay Kumar Verma,[abcd] Shamma Jain,[ab] Kishor Kumar Johari,[ab] Christophe Candolfi,[e] Bertrand Lenoir,*[e] Sumeet Walia,[cd] S. R. Dhakate[ab] and Bhasker Gahtori*[ab]

Received 29th October 2023,
Accepted 15th November 2023

DOI: 10.1039/d3ma00923h

rsc.li/materials-advances

Half-Heusler (HH) alloys based on TiCoSb are becoming popular semiconducting materials for mid-temperature thermoelectric (TE) applications, due to their superior Seebeck coefficient, moderate electrical conductivity, and excellent mechanical properties. However, their practical applicability is mainly limited by their high lattice thermal conductivity. Here, we show how a multi-alloying approach that involves co-substitution of Zr and Hf on the Ti site and Bi on the Sb site can significantly lower the heat transport of the $TiCo_{0.85}Fe_{0.15}Sb$ alloy due to enhanced mass and strain-field fluctuations in the lattice. The substantial rise in point-defect phonon scattering leads to a sharp reduction in the lattice thermal conductivity from 8 to 2 W m^{-1} K^{-1} at ~300 K and from 5 to 1.74 W m^{-1} K^{-1} at ~843 K in $Ti_{0.5}Zr_{0.2}Hf_{0.3}Co_{0.85}Fe_{0.15}Sb_{0.96}Bi_{0.4}$. The achieved thermal conductivity is the lowest value reported so far among TiCoSb-based alloys. Importantly, the reduction in thermal conductivity outweighs the concomitant decrease in the power factor, ultimately leading to an improved thermoelectric figure of merit *ZT*. Our findings show that creating large point defects through heavy isovalent substitution is an effective approach to significantly reduce the phonon transport in HH alloys.

Introduction

The investigation of thermoelectric (TE) materials has accelerated during the past two decades, and optimized compounds have been incorporated into thermoelectric devices that can be utilized for both cooling and green power production.[1] Performance of a TE device mainly depends on a dimensionless parameter, the thermoelectric figure of merit $ZT = \frac{\alpha^2\sigma T}{\kappa_L + \kappa_e}$, where α is the Seebeck coefficient, σ is the electrical conductivity, $\alpha^2\sigma$ is the power factor (PF), T is absolute temperature, κ_L is the lattice thermal conductivity and κ_e is the electronic contribution to the thermal conductivity. However, due to the fact that α, σ, and κ_e are highly reliant upon one another *via* the carrier concentration, the electronic band structure, and the scattering processes, the design of highly efficient thermoelectric materials has been a persistently difficult task.[2,3] The general strategy to enhance the power factor includes optimization of carrier concentration by doping,[4,5] and electronic band engineering.[6,7] Due to the independency of κ_L on electronic transport, limiting the propagation of heat-carrying acoustic phonons can be realized by various approaches[8] that notably include point-defect (atomic scale alloying) scattering,[9,10] bonding effect,[11,12] edge dislocations,[13,14] grain boundaries,[15,16] nano-sized grains, and the formation of *in situ* inclusion of nano precipitates in the host material.[17,18]

In addition to chalcogenides,[19,20] skutterudites,[21,22] silicides[23,24] and clathrates[25,26] extensively studied over the last decade for power generation applications, half-Heuslers (HH) alloys are promising candidates owing to their decent thermoelectric performance, low cost, composed *via* environmentally-friendly elements, good thermal stability and high mechanical robustness.[27–30] The cubic crystal structure of HH compounds with the *XYZ* stoichiometry is built up by four interpenetrated

[a] *CSIR-National Physical Laboratory, Dr. K. S. Krishnan Marg, New Delhi 110012, India. E-mail: bhasker@nplindia.org; Fax: +91-11-45609310; Tel: +91-11-45608556*
[b] *Academy of Scientific & Innovative Research (AcSIR), Ghaziabad, 201002, India*
[c] *Functional Materials and Microsystems Research Group and the Micro Nano Research Facility, RMIT University, Melbourne, VIC 3001, Australia*
[d] *School of Engineering, RMIT University, GPO Box 2476, Melbourne, Victoria 3001, Australia*
[e] *Institut Jean Lamour UMR 7198 CNRS – Université de Lorraine Campus ARTEM, 2 allée André Guinier, BP 50840, Nancy 54011, France. E-mail: bertrand.lenoir@univ-lorraine.fr*

† Electronic supplementary information (ESI) available. See DOI: https://doi.org/10.1039/d3ma00923h

face-centered cubic (fcc) lattices with one vacant position. Semiconducting properties generally emerge when the chemical composition is valence-balanced. Both n-(XNiSn; X = Ti, Zr or Hf) and p-type (XCoSb and X′FeSb; X = Ti, Zr or Hf and X′ = Nb or Ta) compositions can be designed to achieve high thermoelectric performance *via* proper optimization. More complex compositions such as vacancy-containing $X'_{0.8}CoSb$, double, triple and high-entropy HHs have been recently studied, providing interesting avenues to engineer novel compositions with improved thermoelectric performance.[31–33]

Among these compositions, TiCoSb-based alloys have received significant attention because of the tuning ability to develop both n- and p-type compatible counterparts with similar thermal expansion coefficients which are prerequisite for TE devices. TiCoSb has complex electronic band structure that can be engineered to increase valley degeneracy, which contributes to the high power factors achieved in p-type alloys.[7] However, high κ_L is one of the key factors that restricts the TE performance of TiCoSb based compounds. Significant efforts were devoted to lowering κ_L using various approaches such as doping,[34] nanostructuring[35] or nano-composite.[36] The possibility to parallel enhance point-defect scattering through atomic substitutions and induce electronic band convergence in p-type TiCoSb alloys have been demonstrated in recent studies, yielding decreased κ_L values of 2.5 W m^{-1} K^{-1} at 823 K in $Ti_{0.8}Zr_{0.2}Co_{0.85}Fe_{0.15}Sb_{0.96}Sn_{0.04}$.[37] The resulting improved maximum *ZT* value of 0.54 at 823 K places this alloy among the best reported p-type TiCoSb-based compositions without phase separation.

In this work, we explore alternative routes to further reduce κ_L by creating additional point defects in p-type $TiCo_{0.85}Fe_{0.15}Sb$ *via* heavy substitution on the Ti and Sb sites with Zr/Hf and Bi, respectively. These substitutions enhance mass and strain field fluctuations in the lattice which drive a significant decrease in κ_L of ∼65%, eventually reaching ∼1.74 W m^{-1} K^{-1} at 843 K for $Ti_{0.5}Hf_{0.3}Zr_{0.2}Co_{0.85}Fe_{0.15}Sb_{0.96}Bi_{0.04}$. This reduced heat transport improves the *ZT* values by ∼60% compared to $TiCo_{0.85}Fe_{0.15}Sb$, leading to a peak *ZT* value of ∼0.3 at 843 K. Not only do these findings further demonstrate the benefit from heavy alloying to reduce the phonon heat transport in HH alloys but they also indicate the importance of carefully choosing the substituting elements to maintain the convergence of the valence band edges in TiCoSb alloys.

Experimental details

All the samples with chemical compositions $Ti_{0.5}Hf_{0.3}Zr_{0.2}Co_{0.85}Fe_{0.15}Sb_{1-x}Bi_x$ (x = 0–0.04) were synthesized by weighing stoichiometric quantities of high-purity Ti granules (99.9%), Co pieces (99.9%), Sb shots (99.9999%), Zr foil (99.8%), Hf powders (99.6%), Fe powders (99+%) and Bi powders (99.999%), all purchased from Alfa Aesar. As a first step, a solid pellet composed of mixed powders of Hf, Fe, and Bi was cold-pressed. This pellet and the remaining elements were combinedly arc melted and alloyed using an arc-melter (Edmund Bühler GmbH, MAM-1) under argon atmosphere. To achieve homogeneous stoichiometry, melting done be several times with flipping the ingots. The melted ingots were first crushed into fine powders, then placed into a graphite die, and then processed to a spark plasma sintering (Dr Sinter, 725) system at a temperature of 1373 K with a constant pressure of 50 MPa, that route was optimized in our previous study.[38] The density d of each polished sample was measured based on the Archimedes' principle using a Mettler Toledo apparatus (model ML204/A01).

Patterns of powder X-ray diffraction (PXRD) were acquired at room temperature for each of the samples by using an X-ray diffractometer (Rigaku Miniflex II). The PXRD data have been performed for Rietveld refinements using the FullProf software.[39] The field-emission scanning electron microscope (FESEM, TESCAN MAGNA GMH) and the energy-dispersive X-ray spectroscopy (EDS, EDAX OCTANE ELECT SUPER) were used to investigate the surface morphology and chemical homogeneity, respectively. In order to further investigate microstructural features at the atomic scale, high-resolution transmission electron microscopy (HRTEM; JEM 2100F-JOEL 200 kV) was performed.

Electrical resistivity and Seebeck coefficient were simultaneously measured with a ZEM-3 system (ULVAC-RIKO) in the temperature range of 300 to 823 K. The Hall carrier density p_H and mobility μ_H were measured at room temperature using a Hall effect instrument (HEMS, Nanomagnetics). Using sapphire as a standard and a differential scanning calorimeter system (DSC-NETZSCH, 404 F3), the isobaric specific heat (c_p) of each sample was determined between 300 and 773 K. The thermal diffusivity (D) of disk-shaped samples was measured by employing a laser flash method (Netzsch LFA 427). The total thermal conductivity κ (= κ_L + κ_e) was calculated using the relation $\kappa = c_p D d$.

Result and discussion

The PXRD patterns of the synthesized samples $Ti_{0.5}Hf_{0.3}Zr_{0.2}Co_{0.85}Fe_{0.15}Sb_{1-x}Bi_x$ ($0 \le x \le 0.04$) are exhibited in Fig. 1(a). The diffraction peaks reflect the cubic crystal structure of HH phase for each sample. Rietveld refinements against the PXRD data, performed for each sample with an illustrative example for x = 0.04 shown in Fig. 1(b), confirm the absence of obvious impurity within the detection limit of this technique. The Rietveld refined parameters of each sample are listed in Table S1 in ESI.†

The surface morphology and elemental chemical configuration of the illustrative sample $Ti_{0.5}Hf_{0.3}Zr_{0.2}Co_{0.85}Fe_{0.15}Sb_{0.96}Bi_{0.04}$ were investigated by FESEM and EDXS as depicted in Fig. 2. The FESEM images show that the sample is densely packed with the presence of few minor secondary phases in the HH matrix. The chemical compositions (Fig. 2(b)), corresponding to the broad area shown in Fig. 2(a), is very close to the nominal stoichiometry. The minor secondary phase

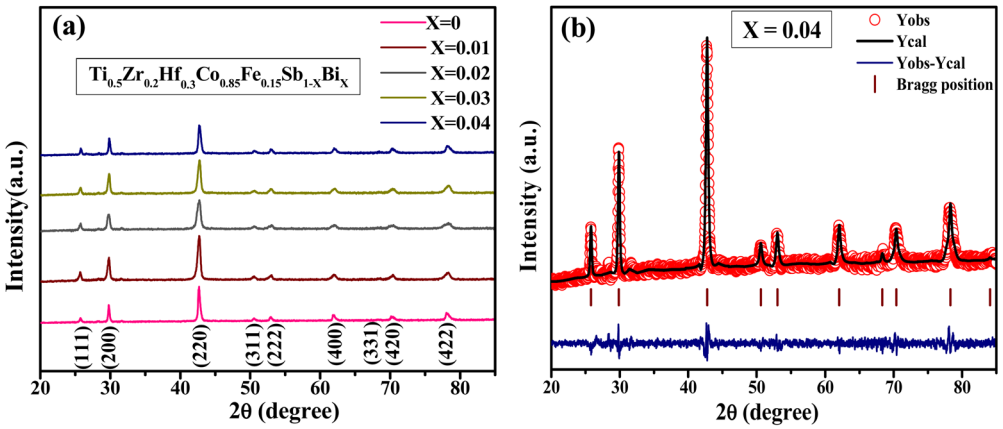

Fig. 1 (a) Room-temperature PXRD patterns and (b) Rietveld refinement performed on the illustrative sample $Ti_{0.8}Zr_{0.2}Hf_{0.3}Co_{0.85}Fe_{0.15}Sb_{0.96}Bi_{0.04}$.

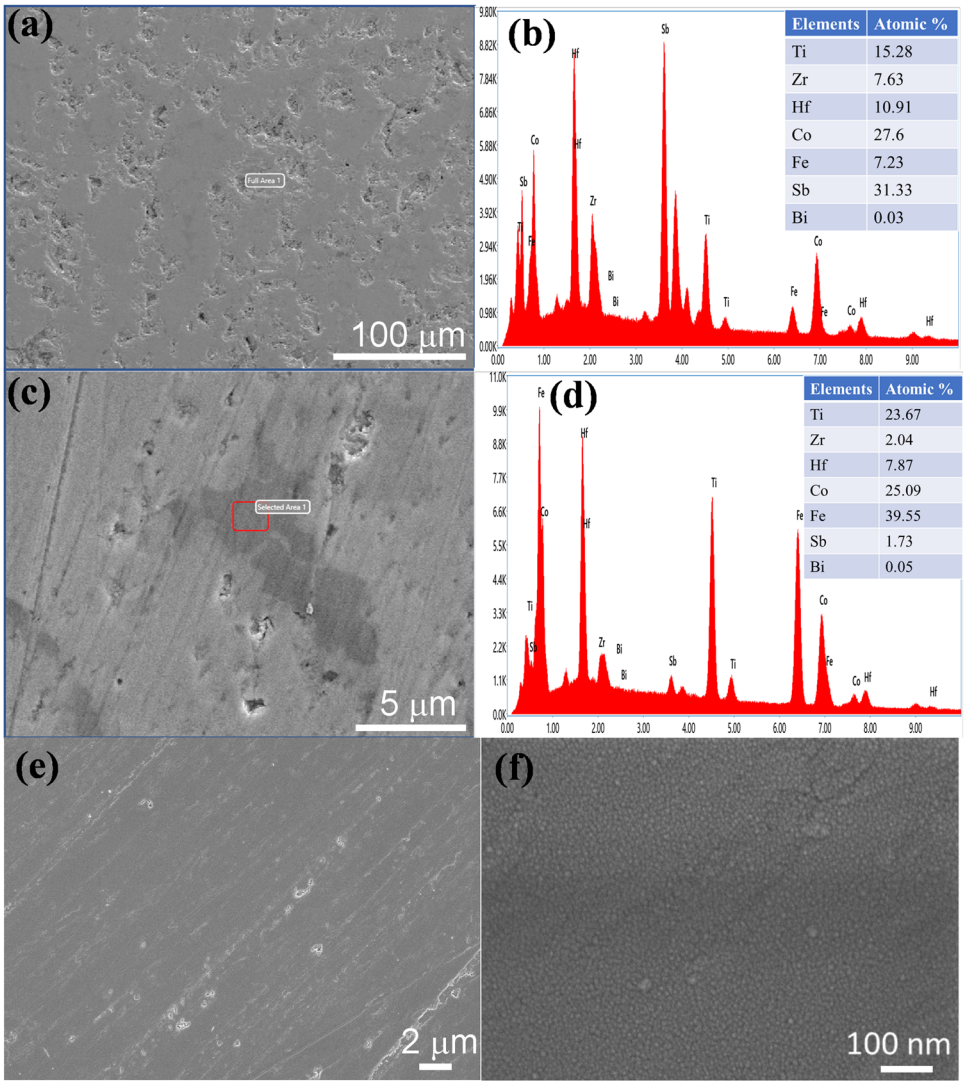

Fig. 2 FESEM and EDXS data for the illustrative sample $Ti_{0.5}Zr_{0.2}Hf_{0.3}Co_{0.85}Fe_{0.15}Sb_{0.96}Bi_{0.04}$, (a) and (b) FESEM image along with EDXS spectra of full image, (c) and (d) FESEM image and EDXS spectra of dark contrast region, and (e) and (f) FESEM image of the alumina-polished sample at low and high magnification.

observed in Fig. 2(c) corresponds to a Fe-rich phase (Fig. 2(d), dark contrast region). Fig. 2(d) and (e) show the FESEM images of alumina-polished samples at low and high resolution, which confirm their high density. The elemental mapping of the representative sample x = 0.04 (Fig. S1 in ESI†) confirms the uniform distribution of the elements with only the Fe-rich phase as a minor secondary phase.

To further investigate the microstructure at the atomic scale, HRTEM analysis of the representative sample $Ti_{0.5}Hf_{0.3}Zr_{0.2}Co_{0.85}Fe_{0.15}Sb_{0.96}Bi_{0.04}$ was carried out (Fig. 3). The extracted interplanar spacing of the lattice planes are in good agreement with that of the TiCoSb HH phase. Two regions, R1, and R2 were analyzed at the atomic scale. The region R1 consists of a plane of calculated d-spacings 0.2117 nm nearly corresponding to the (220) family of planes, which is more dominating in TiCoSb HH phase as found in XRD data. Moreover, the edge dislocation defects are observed in region R1, while the region R2 consists of four overlapping planes of d-spacing 0.2845 nm, 0.2117 nm, 0.1885 nm, and 0.158 nm, which are nearly corresponding to (200), (220), (311), and (400) family of planes of TiCoSb HH phase, and also show the edge dislocations. The analyses demonstrate the presence of a large distribution of edge dislocation defects, which are expected to impact the transport properties. Fig. 3(b) shows the selected area electron diffraction (SAED) pattern of the same sample, where the superimposition of bright spots with Debye rings, are clearly visible, confirming the polycrystalline nature of the material.[40] The diffraction pattern reflects the material's crystal structure in the reciprocal space where Debye rings are found corresponding to the family of planes (111), (200), (220), (222), (400), (311), (422) of TiCoSb HH phase.

Fig. 4 illustrates the temperature dependence of the electronic transport parameters of all the samples $Ti_{0.5}Hf_{0.3}Zr_{0.2}Co_{0.85}Fe_{0.15}Sb_{1-x}Bi_x$ ($0 \leq x \leq 0.04$). In order to facilitate a valuable comparison, the transport parameters of $TiCo_{0.85}Fe_{0.15}Sb$, which were determined in a previous experiment, have been included.[7] At 300 K, σ tends to decrease in samples alloyed with Zr and Hf with respect to $TiCo_{0.85}Fe_{0.15}Sb$. Further alloying with Bi ($0 \leq x \leq 0.04$) weakly affects σ due to the small concentration of Bi introduced on the Sb site. The increasing trend of σ with increasing temperature indicates semiconducting behavior of all samples. Hall effect measurements carried out at 300 K (Table 1) reveal that the hole concentration p_H drops from 5.4 to 1.2 $\times$ 10^{20} cm^{-3} as the Bi content increases. A similar behavior of decreased carrier density upon isoelectronic Bi doping on Sb has also been observed in other p-type compounds.[41,42] The corresponding hole mobilities μ_H remain very low, varying in the range 0.68–1.57 $cm^2\ V^{-1}\ s^{-1}$ at 300 K. These values are similar to those achieved in other heavily-alloyed HH compounds[43] and can be mainly ascribed to alloy scattering that strongly limits hole mobility.

The temperature dependence of the weighted mobility (μ_w) was calculated using the measured σ and α:[44]

$$\mu_w = \frac{3h^3\sigma}{8\pi e(2m_e k_B T)^{3/2}} \times \left[\frac{\exp\left[\frac{|\alpha|}{k_B/e} - 2\right]}{1+\exp\left[-5\left(\frac{|\alpha|}{k_B/e} - 1\right)\right]} + \frac{\frac{3}{\pi^2}\frac{|\alpha|}{k_B/e}}{1+\exp\left[5\left(\frac{|\alpha|}{k_B/e} - 1\right)\right]}\right]$$

where h is the Planck constant, e is the electronic charge, m_e is the bare electron mass and k_B is the Boltzmann constant. The temperature dependent μ_w of all samples, shown in Fig. 4(b), indicates that μ_w is significantly reduced upon Zr and Hf alloying while it remains less affected by the substitution of Bi for Sb due to its low concentration. This reduction in μ_w can

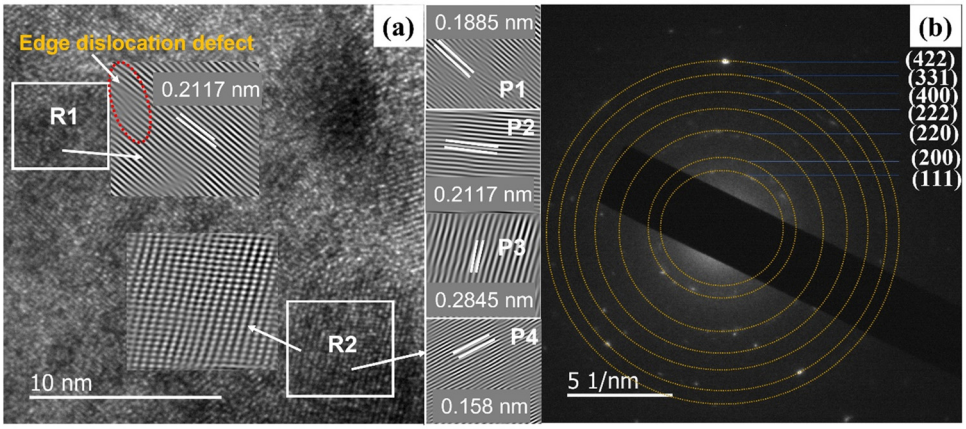

Fig. 3 HRTEM analysis of the $Ti_{0.5}Hf_{0.3}Zr_{0.2}Fe_{0.15}Co_{0.85}Sb_{0.96}Bi_{0.04}$ sample. (a) HRTEM image, where regions further analyzed are indicated. The Fast Fourier Transform (FFT) and Inverse Fast Fourier Transform (IFFT) of the regions R1, and R2 are shown. Region R2 consist of four planes named as P1, P2, P3, and P4. Edge dislocation defects are found in both R1 and R2 regions, (b) selected area electron diffraction (SAED) pattern evidencing the polycrystalline nature of the sample.

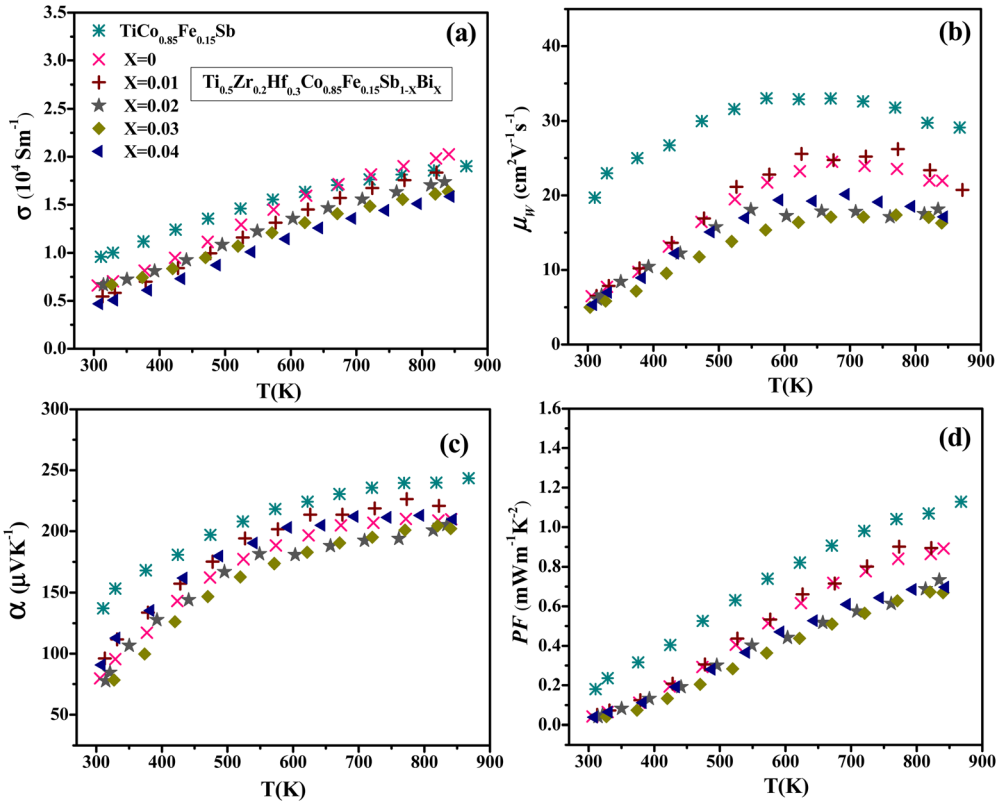

Fig. 4 Temperature dependent electronic transport properties of samples $Ti_{0.5}Zr_{0.2}Hf_{0.3}Co_{0.85}Fe_{0.15}Sb_{1-x}Bi_x$ (x = 0–0.04), (a) electrical conductivity σ, (b) weighted mobility μ_w, (c) Seebeck coefficient α and (d) power factor PF.

Table 1 Table 1 The room temperature Hall data of all samples $Ti_{0.8}Zr_{0.2}Hf_{0.3}Co_{0.85}Fe_{0.15}Sb_{1-x}Bi_x$

Parameters	X = 0	X = 0.01	X = 0.02	X = 0.03	X = 0.04
Hole density p_H ($\times 10^{20}$ cm^{-3})	5.40	4.68	1.54	2.59	1.21
Mobility μ_H (cm^2 V^{-1} s^{-1})	0.68	0.67	1.36	1.38	1.57

be ascribed to the heavy alloying at the Ti site and the low density-of-states effective mass (m^*_{DOS}, see below), in comparison to other reported p-type TiCoSb compositions with improved electronic properties (Fig. S2, ESI†).

Fig. 4(c) displays the temperature-dependent Seebeck coefficient α for each sample. The positive value of α over the entire temperature range indicates an electrical conduction dominated by holes. The room-temperature α values significantly decrease upon Zr and Hf alloying from 137 to 80 μV K^{-1} in spite of the concomitant decrease in the Hall carrier density. This counterintuitive trend might be rationalized through modifications of the electronic band structure and, in particular, to an increase in the energy offset between the valence band maxima located at the Γ and L points of the Brillouin zone. The energy offset of 51 meV in TiCoSb can be manipulated by alloying on the Co and Sb sites, which modifies the energy of the band edges at the L and Γ point, respectively. In contrast to Fe and Sn doping in $TiCo_{0.85}Fe_{0.15}Sb$ that promotes band convergence,[7] Zr and Hf might tend to induce the opposite effect. This trend suggests that the Ti orbitals mainly control the energy of the valence band edge at the Γ point, as evidenced in the ZrNiSn, NbCoSn and NbFeSb HH alloys by electronic band structure calculations.[6] The isovalent substitution of Bi for Sb only weakly affects the α values at 300 K with values ranging between 78 and 96 μV K^{-1}, indicating that Bi is either ineffective in inducing band convergence or that the highest concentration considered herein remains too low to observe any beneficial influence. At high temperatures, α tends to saturate, a behavior that can be ascribed to minority carrier excitation across the electronic band gap due to thermal energy.

These lowered α values are responsible for the decrease in the power factor PF = $\alpha^2\sigma$ over the entire temperature range with respect to the values achieved in $TiCo_{0.85}Fe_{0.15}Sb$ and in $TiCo_{0.85}Fe_{0.15}Sb_{1-x}Sn_x$[7] (Fig. 4(d)). Alloying with Bi has virtually no effect on PF at 300 K, while a marginal decrease is observed at higher temperatures.

The temperature dependence of the total thermal conductivity κ of each sample $Ti_{0.5}Hf_{0.3}Zr_{0.2}Co_{0.85}Fe_{0.15}Sb_{1-x}Bi_x$ ($0 \leq x \leq 0.04$) is shown in Fig. 5(a). A sharp decrease in $\kappa \sim 62\%$ at 300 K and $\sim$47% at $\sim$850 K is achieved upon Zr and Hf alloying with respect to $TiCo_{0.85}Fe_{0.15}Sb$. The addition of Bi further lowers κ by $\sim$29% to reach $\sim$2 W m^{-1} K^{-1} at $\sim$850 K in $Ti_{0.5}Hf_{0.3}Zr_{0.2}Co_{0.85}Fe_{0.15}Sb_{0.96}Bi_{0.04}$. This substantial reduction in thermal conductivity is due to the enhanced disorder induced by these substitutions. As shown in Fig. 5(b), which presents a comparison with the current literature on both

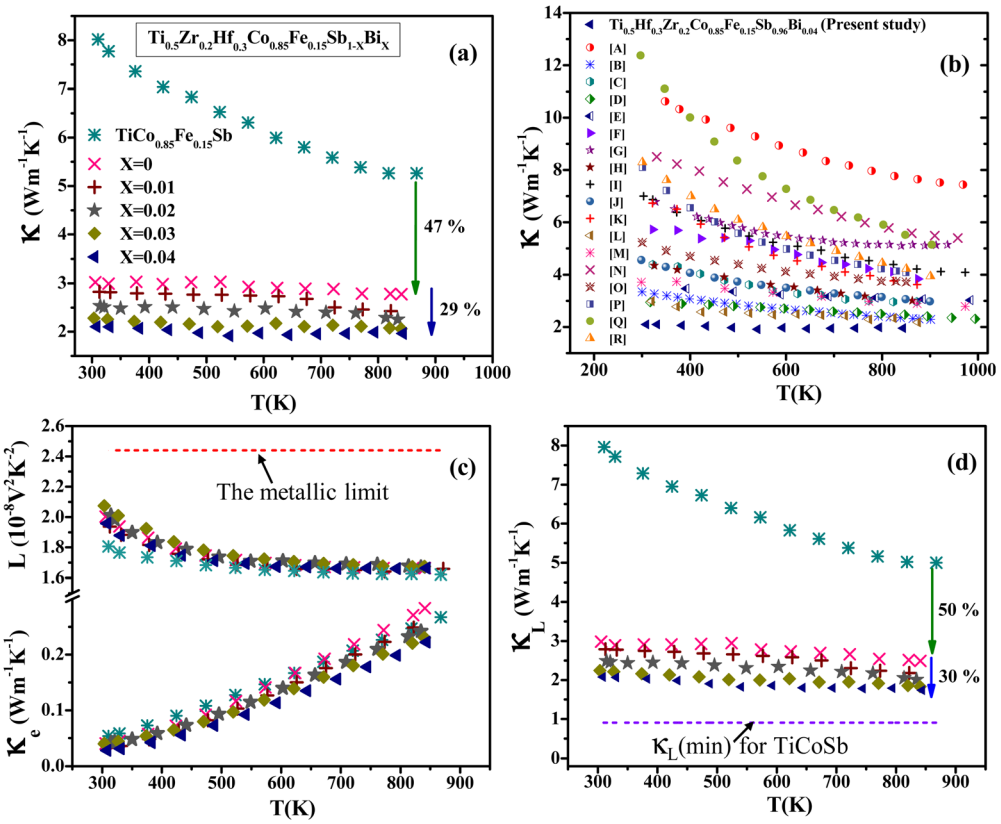

Fig. 5 Temperature dependence of the (a) total thermal conductivity κ. (b) Comparison of κ of various TiCoSb-based HH alloys, with [A]-TiCoSb,[45] [B]-$Ti_{0.5}Zr_{0.25}Hf_{0.25}Co_{0.95}Ni_{0.05}Sb$,[46] [C]-$TiCo_{1.05}Sb_{0.8}Sn_{0.2}$,[35] [D]-$Ti_{0.6}Hf_{0.4}CoSb_{0.8}Sn_{0.2}$,[47] [E]-$Ti_{0.5}Hf_{0.5}CoSb_{0.8}Sn_{0.2}$,[48] [F]-$Ti_{0.9}Nb_{0.1}CoSb$,[49] [G]-$Ti_{0.8}Nb_{0.1}Ta_{0.1}CoSb_{0.8}Sn_{0.2}$,[50] [H]-$Ti_{0.341}Zr_{0.343}Hf_{0.316}Co_{0.957}Pd_{0.043}Sb$,[51] [I]-$TiCoNi_{0.2}Sb$,[52] [J]-$Ti_{0.6}Hf_{0.4}Co_{0.87}Ni_{0.13}Sb$,[53] [K]-$TiCoSb_{0.8}Sn_{0.2}$,[54] [L]-$Ti_{0.6}Zr_{0.4}CoSb_{0.8}Sn_{0.2}$,[54] [M]-$Ti_{0.5}Hf_{0.4}Ta_{0.1}CoSb$,[34] [N]-$TiCoSb_{0.9}Sn_{0.1}$,[55] [O]-$TiFe_{0.3}Co_{0.7}Sb$,[56] [P]-$TiCoGe_{0.2}Sb_{0.8}$,[57] [Q]-$TiCo_{0.9}Ni_{0.1}Sb$,[58] [R]-$Ti_{0.92}Ta_{0.08}CoSb$,[59] (c) Lorenz number L, electronic thermal conductivity κ_e and (d) lattice thermal conductivity κ_L. In panels (c) and (d), the horizontal dashed lines stand for the degenerate limit of L and the minimum lattice thermal conductivity $\kappa_{L,min}$, respectively.

n- and p-type TiCoSb-based alloys, this value is among the lowest ever obtained in TiCoSb-based alloys.

To further shed light on the influence of this heavy alloying on the heat transport, κ was decoupled into the electronic thermal conductivity κ_e and lattice thermal conductivity κ_L (Fig. 5(c) and (d)). κ_e was estimated according to the Wiedemann–Franz law $\kappa_e = L\sigma T$, where L is the Lorenz number. L was calculated by the relation $L = 1.5 + \exp(-|\alpha|/116)$ where L and α are expressed in 10^{-8} V^2 K^{-2} and μV K^{-1}, respectively.[60] The L values are significantly lower than the degenerate limit L_0 of 2.44×10^{-8} V^2 K^{-2} and monotonically decrease with increasing temperature for each sample, as is frequently seen in heavily-doped semiconductors. Fig. 5(c) demonstrates that κ_e increases with temperature and does not vary significantly with the substitution of Bi for Sb. The lattice thermal conductivity $\kappa_L = \kappa - \kappa_e$ decreases by $\sim$50% to reach $\sim$2.49 W m^{-1} K^{-1} at 843 K upon alloying on the Ti site. The κ_L is further reduced by Bi substitution, leading to the lowest κ_L value of $\sim$1.74 W m^{-1} K^{-1} achieved at 843 K in the sample $Ti_{0.5}Hf_{0.3}Zr_{0.2}Co_{0.85}Fe_{0.15}Sb_{0.96}Bi_{0.04}$ (Fig. 5(d)). This lowest value is approaching the minimum limit $\kappa_{L\,min}$ = 0.907 W m^{-1} K^{-1}, which was calculated for TiCoSb using the model developed by Cahill and Pohl[61] (see equations in ESI†). The drop in κ_L over the whole temperature range primarily stems from the large enhancement in point-defect scattering caused by the substitutions of Zr, Hf, and Bi for Ti and Sb, respectively, which yield a pronounced increase in the mass and strain field fluctuations.

To further investigate the role played by these substitutions on κ_L, the Debye–Callaway model that depends on the relaxation time approximation and assuming the absence of dispersion in the vibrational spectrum with no variations between the longitudinal and transverse polarizations, was considered.[62,63] The correction factor for phonon–phonon interactions is not taken into account in the simplified form of this model, which yields the following equation:[63,64]

$$\kappa_L = \frac{k_B}{2\pi^2 v}\left(\frac{k_B T}{\hbar}\right)^3 \int_0^{\theta_D/T} \frac{x^4 e^x}{\tau^{-1}(e^x-1)^2} dx$$

where $x = \hbar\omega/k_B T$, $\hbar = h/2\pi$, is the reduced Planck constant, ω represents the phonon frequency, the total relaxation time of all scattering processes is represented by τ, θ_D is the Debye temperature, and $\omega_D = k_B T/\hbar$ is the Debye frequency. The average sound velocity $v = \left\{\frac{1}{3}\left(\frac{1}{v_L^3} + \frac{2}{v_T^3}\right)\right\}^{-1/3}$ and atom density n were used to calculate θ_D according to the equation

$\theta_D = v(6\pi^2 N)^{1/3}/k_B$.[64] Taking the values for the sound velocities used to calculate $\kappa_{L\,min}$ yield $v = 3597$ m s^{-1} and $\theta_D = 417$ K.[65] By following Matthiessen's rule, τ can be determined by summing the inverses of the various scattering relaxation times $\tau^{-1} = \sum \tau_i^{-1}$, where τ_i denotes the relaxation time of the ith scattering process. Here, point-defect (PD) scattering, Umklapp (U) scattering, and boundary (B) scattering were taken into account for the calculation of κ_L. The details of these calculations can be found in the ESI.†

Fig. 6(a) shows the disorder scattering parameters Γ_M, Γ_S, and Γ for all samples. All these parameters abruptly rise in the samples alloyed with Zr and Hf, indicating enhanced mass and strain field fluctuations in the crystal lattice due to the pronounced differences in atomic mass and size between Zr, Hf, and Ti. Moreover, a monotonic increase in Γ_M, Γ_S, and Γ is observed in the Bi-substituted samples, which favors further lowering in κ_L. The calculated value of Grüneisen parameter γ of each sample (Fig. S3 in the ESI†) shows a peak value of 3.4 for the alloy $Ti_{0.5}Hf_{0.3}Zr_{0.2}Co_{0.85}Fe_{0.15}Sb_{0.96}Bi_{0.04}$, which is higher than that determined for $TiCo_{0.85}Fe_{0.15}Sb$. These high γ values are indicative of effective phonon–phonon scattering, which is a contributing factor to reduce κ_L.[66]

The relaxation time of various scattering mechanisms as a function of phonon frequency is depicted in Fig. S4 of the ESI.† The relaxation time curves for different scattering have been calculated for the representative sample $Ti_{0.5}Hf_{0.3}Zr_{0.2}Co_{0.85}Fe_{0.15}Sb_{0.96}Bi_{0.04}$ at 450 K (higher than Debye temperature of TiCoSb), assuming that all the vibrational modes have been populated at this temperature and contribute to phonon scattering. High-frequency phonons are scattered primarily by point defects and Umklapp processes, while low-frequency phonons are scattered mostly by grain boundaries.[62,64] These predictions have been proven in the current set of alloys, where it was shown that grain boundary scattering is important at low frequency but point defect and Umklapp phonon scattering dominate at high frequency. The point-defect scattering mechanism shows the minimal relaxation time of $\tau_{PD} \sim 1 \times 10^{-14}$ s when it is excited at the Debye frequency, indicating that this mechanism outweighs the other processes and is predominantly responsible for the suppression in κ_L observed

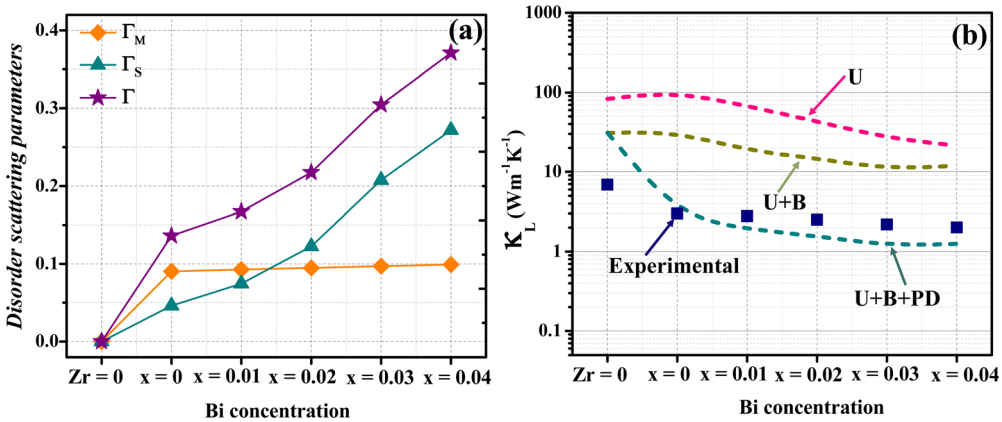

Fig. 6 Interplay of phonon scattering processes within the Debye–Callaway model for the $Ti_{0.5}Zr_{0.2}Hf_{0.3}Co_{0.85}Fe_{0.15}Sb_{1-x}Bi_x$ alloys at 450 K. (a) Mass, strain and experimental disorder scattering parameters Γ_M, Γ_S and Γ, respectively. The label "Zr = 0" refers to the Zr, Hf, and Bi-free sample $TiCo_{0.85}Fe_{0.15}Sb$. (b) Comparison of the experimental and calculated lattice thermal conductivity κ_L by considering different phonon scattering processes.

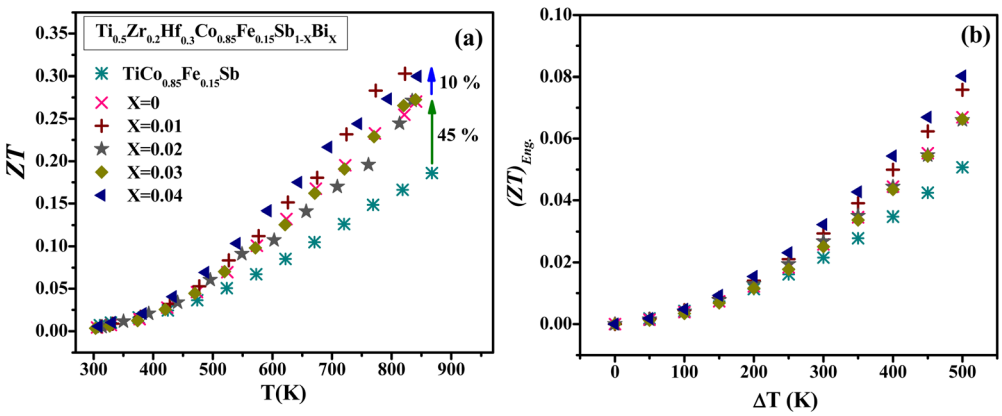

Fig. 7 (a) Temperature dependence of the dimensionless thermoelectric figure of merit ZT. (b) Engineering thermoelectric figure of merit $(ZT)_{Eng}$ as a function of the temperature difference ΔT of $Ti_{0.5}Zr_{0.2}Hf_{0.3}Co_{0.85}Fe_{0.15}Sb_{1-x}Bi_x$.

experimentally. Fig. 6(b) shows the calculated κ_L for different combinations of scattering mechanisms, that is, (U), (U + PD) and (U + PD + B). The κ_L values measured at 450 K for all samples have also been added in Fig. 6(b). The combination of the three scattering mechanisms (U + PD + B) yields a good agreement, indicating that all these scattering mechanisms are influencing the heat transport in these alloys.

Fig. 7(a) shows the temperature dependence of the dimensionless thermoelectric figure of merit *ZT*. The co-substitution of Zr and Hf for Ti leads to a significant rise in the *ZT* values with a peak *ZT* of 0.27 at 843 K, which is ~47% higher than that of parent alloy $TiCo_{0.85}Fe_{0.15}Sb$. The significant lowering in κ_L is the key factor behind this *ZT* improvement, which counterbalances the reduction in the power factor. The small concentration of Bi does not significantly impact the *ZT* values that reaches the moderate value of 0.3 at 843 K in the $Ti_{0.5}Hf_{0.3}Zr_{0.2}Fe_{0.15}Co_{0.85}Sb_{0.96}Bi_{0.04}$ alloy. Finally, the engineering figure of merit $(ZT)_{Eng}$ was calculated as a function of the temperature difference ΔT within the cumulative temperature dependency (CTD) model (see ESI† for detailed information). $(ZT)_{Eng}$ increases with Zr, Hf and Bi doping, confirming that the reduction in thermal conductivity outweighs the decrease in the electronic properties. The peak $(ZT)_{Eng}$ value of ~0.08 for ΔT = 500 K is realized for the x = 0.04 sample, which is ~60% greater than that determined for $TiCo_{0.85}Fe_{0.15}Sb$ as shown in Fig. 7(b).

Conclusion

In the present study, a pronounced drop in the lattice thermal conductivity of the HH alloy TiCoSb has been successfully achieved through a heavy isovalent atomic substitution strategy using Zr, Hf and Bi. The strong mass and strain field fluctuations induced by these substitutions led to a large decrease in κ, ultimately reaching ~2 W m^{-1} K^{-1} for the composition $Ti_{0.5}Hf_{0.3}Zr_{0.2}Co_{0.85}Fe_{0.15}Sb_{0.96}Bi_{0.04}$, which is among the lowest values reported so far in n- and p-type TiCoSb-based HH compounds. While this approach is particularly effective in lowering the phonon-mediated heat transport, the accompanying increased atomic disorder has a detrimental influence on the power factor due to the effectively reduced hole mobility and the possible increase in the energy difference between the valence band maxima. Nevertheless, the overall beneficial impact of heavy alloying on the phonon transport outweighs this decrease, yielding a peak *ZT* value of ~0.3 at 843 K in $Ti_{0.5}Hf_{0.3}Zr_{0.2}Co_{0.85}Fe_{0.15}Sb_{0.96}Bi_{0.04}$. Further optimization of the electronic properties may be achieved by varying the Co-to-Fe ratio or substituting Sn for Sb, thereby helping to maintain the low lattice thermal conductivity while optimizing the power factor by bringing the valence band manifold closer to band convergence.

Author contributions

Ajay Kumar Verma: synthesis, characterization, methodology, data analysis and original drafting of the manuscript. Shamma Jain: methodology, and formal analysis. Kishor Kumar Johari: review and editing. Christophe Candolfi: investigation, review, and editing. Bertrand Lenoir: investigation, review, and editing. Sumeet Walia: review, editing and supervision. Sanjay R. Dhakate: review, editing and supervision. Bhasker Gahtori: conceptualization, visualization, review, editing and supervision.

Conflicts of interest

There are no conflicts to declare.

Acknowledgements

The authors would like to express their gratitude to Director, CSIR-NPL, New Delhi, India for his encouragement and support. AKV and SJ would like to express gratitude for the financial support provided by UGC-India. KKJ wishes to express gratitude for the financial support offered by CSIR-India. The authors appreciate the technical assistance provided by Mr Radhey Shyam and Dr Naval Kishor Upadhyay. We also acknowledge Dr J. S. Tawale for the FESEM and EDS measurements. The authors are thankful to Mr Abhishek for plagiarism check utilizing the software iThenticate available in the library of CSIR-NPL, New Delhi, India.

References

1 N. Jaziri, *et al.*, A comprehensive review of Thermoelectric Generators: Technologies and common applications, *Energy Rep.*, 2020, **6**, 264–287.
2 J. Mao, *et al.*, Advances in thermoelectrics, *Adv. Phys.*, 2018, **67**(2), 69–147.
3 L. You, *et al.*, Realization of higher thermoelectric performance by dynamic doping of copper in n-type PbTe, *Energy Environ. Sci.*, 2019, **12**(10), 3089–3098.
4 E. Rausch, *et al.*, Charge carrier concentration optimization of thermoelectric p-type half-Heusler compounds, *APL Mater.*, 2015, **3**(4), 041516.
5 C. Bhandari and D. M. Rowe, Optimization of carrier concentration, in *CRC handbook of thermoelectrics*, CRC Press, 2018, pp. 43–54.
6 S. Guo, *et al.*, Conduction band engineering of half-Heusler thermoelectrics using orbital chemistry, *J. Mater. Chem. A*, 2022, **10**(6), 3051–3057.
7 A. K. Verma, *et al.*, Realization of Band Convergence in p-Type TiCoSb Half-Heusler Alloys Significantly Enhances the Thermoelectric Performance, *ACS Appl. Mater. Interfaces*, 2023, **15**(1), 942–952.
8 C. Chang and L.-D. Zhao, Anharmoncity and low thermal conductivity in thermoelectrics, *Mater. Today Phys.*, 2018, **4**, 50–57.
9 R. He, *et al.*, Improved thermoelectric performance of n-type half-Heusler $MCo_{1-x}Ni_xSb$ (M = Hf, Zr), *Mater. Today Phys.*, 2017, **1**, 24–30.

10 W. Li, *et al.*, Promoting SnTe as an eco-friendly solution for p-PbTe thermoelectric via band convergence and interstitial defects, *Adv. Mater.*, 2017, **29**(17), 1605887.
11 J. He, *et al.*, Accelerated discovery and design of ultralow lattice thermal conductivity materials using chemical bonding principles, *Adv. Funct. Mater.*, 2022, **32**(14), 2108532.
12 J. Ji, *et al.*, Functional-Unit-Based Material Design: Ultralow Thermal Conductivity in Thermoelectrics with Linear Triatomic Resonant Bonds, *J. Am. Chem. Soc.*, 2022, **144**(40), 18552–18561.
13 Z. Chen, *et al.*, Vacancy-induced dislocations within grains for high-performance PbSe thermoelectrics, *Nat. Commun.*, 2017, **8**(1), 1–8.
14 Z. Chen, *et al.*, Lattice dislocations enhancing thermoelectric PbTe in addition to band convergence, *Adv. Mater.*, 2017, **29**(23), 1606768.
15 J. Mao, *et al.*, Phonon scattering by nanoscale twin boundaries, *Nano Energy*, 2017, **32**, 174–179.
16 C. Fu, *et al.*, Enhancing the figure of merit of heavy-band thermoelectric materials through hierarchical phonon scattering, *Adv. Sci.*, 2016, **3**(8), 1600035.
17 W. Kim, Strategies for engineering phonon transport in thermoelectrics, *J. Mater. Chem. C*, 2015, **3**(40), 10336–10348.
18 H. Kim, *et al.*, Strategies for manipulating phonon transport in solids, *ACS Nano*, 2021, **15**(2), 2182–2196.
19 H. Meng, *et al.*, Thermoelectric applications of chalcogenides, in *Chalcogenide*, Elsevier, 2020, pp. 31–56.
20 S. Gautam, *et al.*, Structural, Electronic and Thermoelectric Properties of Bi_2Se_3 Thin Films Deposited by RF Magnetron Sputtering, *J. Electron. Mater.*, 2022, **51**(5), 2500–2509.
21 Z.-Y. Liu, *et al.*, A review of $CoSb_3$-based skutterudite thermoelectric materials, *J. Adv. Ceram.*, 2020, **9**(6), 647–673.
22 R. Bhardwaj, *et al.*, $CoSb_3$ based thermoelectric elements pre-requisite for device fabrication, *Solid State Sci.*, 2022, **129**, 106900.
23 S. Fiameni, *et al.*, Synthesis and characterization of Bi-doped Mg_2Si thermoelectric materials, *J. Solid State Chem.*, 2012, **193**, 142–146.
24 Y.-C. Tseng, *et al.*, Advancing the reliability of thermoelectric materials: A case study of silicides through statistics, *Appl. Phys. Lett.*, 2021, **119**(19), 193903.
25 G. S. Nolas, G. A. Slack and S. B. Schujman, Semiconductor clathrates: A phonon glass electron crystal material with potential for thermoelectric applications, in *Semiconductors and semimetals*, Elsevier, 2001, pp. 255–300.
26 T. Takabatake, *et al.*, Phonon-glass electron-crystal thermoelectric clathrates: Experiments and theory, *Rev. Mod. Phys.*, 2014, **86**(2), 669.
27 N. S. Chauhan, *et al.*, Enhanced thermoelectric performance in p-type ZrCoSb based half-Heusler alloys employing nanostructuring and compositional modulation, *J. Materiomics*, 2019, **5**(1), 94–102.
28 K. K. Johari, *et al.*, In Situ Evolution of Secondary Metallic Phases in Off-Stoichiometric ZrNiSn for Enhanced Thermoelectric Performance, *ACS Appl. Mater. Interfaces*, 2022, **14**(17), 19579–19593.
29 K. K. Johari, *et al.*, The charge carrier density modulation in off-stoichiometric ZrNiSn leads to enhanced thermoelectric performance, *Ceram. Int.*, 2023, **49**(16), 26558–26567.
30 T. Zhu, *et al.*, High efficiency half-Heusler thermoelectric materials for energy harvesting. Advanced Energy, *Materials*, 2015, **5**(19), 1500588.
31 K. Berarma, *et al.*, Opto-electronic, thermodynamic and charge carriers transport properties of $Ta_2FeNiSn_2$ and $Nb_2FeNiSn_2$ double half-Heusler alloys, *Semicond. Sci. Technol.*, 2022, **37**(5), 055013.
32 P.-F. Luo, *et al.*, Alloyed triple half-Heuslers: a route toward high-performance thermoelectrics with intrinsically low lattice thermal conductivity, *J. Mater. Chem. A*, 2023, **11**(16), 9125–9135.
33 K. Chen, *et al.*, Synthesis and thermoelectric properties of high-entropy half-Heusler $MFe_{1-x}Co_xSb$ (M = equimolar Ti, Zr, Hf, V, Nb, Ta), *J. Alloys Compd.*, 2022, **892**, 162045.
34 R.-F. Wang, *et al.*, Enhanced thermoelectric performance of n-type TiCoSb half-Heusler by Ta doping and Hf alloying, *Rare Met.*, 2021, **40**(1), 40–47.
35 N. S. Chauhan, *et al.*, Spinodal decomposition in (Ti, Zr) CoSb half-Heusler: A nanostructuring route toward high efficiency thermoelectric materials, *J. Appl. Phys.*, 2019, **126**(12), 125110.
36 C.-C. Hsu, Y.-N. Liu and H.-K. Ma, Effect of the $Zr_{0.5}Hf_{0.5}CoSb_{1-x}Sn_x/HfO_2$ half-Heusler nanocomposites on the *ZT* value, *J. Alloys Compd.*, 2014, **597**, 217–222.
37 A. K. Verma, *et al.*, Coupling of electronic transport and defect engineering substantially enhances the thermoelectric performance of p-type TiCoSb HH alloy, *J. Alloys Compd.*, 2023, **947**, 169416.
38 A. K. Verma, *et al.*, Role of sintering temperature on electronic and mechanical properties of thermoelectric material: A theoretical and experimental study of TiCoSb half-Heusler alloy, *Mater. Chem. Phys.*, 2022, **281**, 125854.
39 J. Rodríguez-Carvajal, Recent developments of the program FULLPROF. Commission on powder diffraction (IUCr), *Newsletter*, 2001, **26**, 12–19.
40 A. V. Humbe, *et al.*, Rietveld refinement, morphology and superparamagnetism of nanocrystalline $Ni_{0.70-x}Cu_xZn_{0.30}Fe_2O_4$ spinel ferrite, *Ceram. Int.*, 2018, **44**(5), 5466–5472.
41 L. Zhou, *et al.*, Effect of Bi doping on the thermoelectric properties of Zn_4Sb_3, *J. Alloys Compd.*, 2010, **503**(2), 464–467.
42 R. Bhardwaj, *et al.*, Optimization of electrical and thermal transport properties of $Fe_{0.25}Co_{0.75}Sb_3$ Skutterudite employing the isoelectronic Bi-doping, *Intermetallics*, 2020, **123**, 106796.
43 Q. Wang, *et al.*, Enhanced thermoelectric performance in Ti(Fe, Co, Ni)Sb pseudo-ternary half-Heusler alloys, *J. Materiomics*, 2021, **7**(4), 756–765.
44 G. J. Snyder, *et al.*, Weighted mobility, *Adv. Mater.*, 2020, **32**(25), 2001537.
45 T. Sekimoto, *et al.*, Annealing effect on thermoelectric properties of TiCoSb half-Heusler compound, *J. Alloys Compd.*, 2005, **394**(1–2), 122–125.
46 W. Xie, Q. Jin and X. Tang, The preparation and thermoelectric properties of $Ti_{0.5}Zr_{0.25}Hf_{0.25}Co_{1-x}Ni_xSb$ half-Heusler compounds, *J. Appl. Phys.*, 2008, **103**(4), 043711.

47 I. Ioannou, *et al.*, High thermoelectric performance of p-type half-Heusler (Hf, Ti)Co(Sb, Sn) solid solutions fabricated by mechanical alloying, *J. Alloys Compd.*, 2021, **858**, 158330.
48 E. Rausch, *et al.*, Enhanced thermoelectric performance in the p-type half-Heusler (Ti/Zr/Hf) $CoSb_{0.8}Sn_{0.2}$ system via phase separation, *Phys. Chem. Chem. Phys.*, 2014, **16**(46), 25258–25262.
49 A. Vishwakarma, *et al.*, Compositional modulation is driven by aliovalent doping in n-type TiCoSb based half-Heuslers for tuning thermoelectric transport, *Intermetallics*, 2020, **125**, 106914.
50 Y. Kawaharada, *et al.*, High temperature thermoelectric properties of CoTiSb half-Heusler compounds, *J. Alloys Compd.*, 2004, **384**(1–2), 308–311.
51 W. Xie, *et al.*, Synthesis and thermoelectric properties of (Ti, Zr, Hf)(Co, Pd) Sb half-Heusler compounds, *J. Phys. D: Appl. Phys.*, 2009, **42**(23), 235407.
52 L. Liu, *et al.*, Interfacial Decoration Tailoring the Thermoelectric Performance of $TiCoNi_xSb$ Half-Heusler Compounds, *ACS Appl. Energy Mater.*, 2021, **4**(7), 7148–7156.
53 P. Qiu, *et al.*, Enhanced thermoelectric performance by the combination of alloying and doping in TiCoSb-based half-Heusler compounds, *J. Appl. Phys.*, 2009, **106**(10), 103703.
54 N. S. Chauhan, *et al.*, Enhanced thermoelectric performance in Hf-Free p-type (Ti, Zr) CoSb half-heusler alloys, *J. Electron. Mater.*, 2019, **48**(10), 6700–6709.
55 T. Sekimoto, *et al.*, Thermoelectric properties of Sn-doped TiCoSb half-Heusler compounds, *J. Alloys Compd.*, 2006, **407**(1–2), 326–329.
56 T. Wu, *et al.*, Thermoelectric properties of p-type Fe-doped TiCoSb half-Heusler compounds, *J. Appl. Phys.*, 2007, **102**(10), 103705.
57 T. Wu, *et al.*, Effects of Ge doping on the thermoelectric properties of TiCoSb-based p-type half-Heusler compounds, *J. Alloys Compd.*, 2009, **467**(1–2), 590–594.
58 M. Zhou, *et al.*, Effects of partial substitution of Co by Ni on the high-temperature thermoelectric properties of TiCoSb-based half-Heusler compounds, *J. Alloys Compd.*, 2005, **391**(1–2), 194–197.
59 M. Zhou, *et al.*, Moderate-temperature thermoelectric properties of TiCoSb-based half-Heusler compounds $Ti_{1-x}Ta_x$-CoSb, *J. Appl. Phys.*, 2007, **101**(11), 113714.
60 H.-S. Kim, *et al.*, Characterization of Lorenz number with Seebeck coefficient measurement, *APL Mater.*, 2015, **3**(4), 041506.
61 D. G. Cahill, S. K. Watson and R. O. Pohl, Lower limit to the thermal conductivity of disordered crystals, *Phys. Rev. B: Condens. Matter Mater. Phys.*, 1992, **46**(10), 6131.
62 C. M. Bhandari and D. M. Rowe, *Thermal conduction in semiconductors*, Wiley, 1988.
63 J. Callaway, Model for lattice thermal conductivity at low temperatures, *Phys. Rev.*, 1959, **113**(4), 1046.
64 H. Xie, *et al.*, Beneficial contribution of alloy disorder to electron and phonon transport in half-Heusler thermoelectric materials, *Adv. Funct. Mater.*, 2013, **23**(41), 5123–5130.
65 T. Sekimoto, *et al.*, Thermoelectric and thermophysical properties of TiCoSb, ZrCoSb, HfCoSb prepared by SPS, in ICT 2005. 24th International Conference on Thermoelectrics, IEEE, 2005.
66 Y.-L. Pei, *et al.*, High thermoelectric performance of oxyselenides: intrinsically low thermal conductivity of Ca-doped BiCuSeO, *NPG Asia Mater.*, 2013, **5**(5), e47.